

The Radiative and Geometric Properties of Melting First-Year Sea Ice

Nathan J. M. Laxague^{1†}, Christopher J. Zappa¹, Andrew R. Mahoney², John Goodwin³,
Cyrus Harris³, Robert E. Schaeffer³, Roswell Schaeffer Sr.³, Sarah Betcher⁴, Donna D.W.
Hauser⁵, Carson R. Witte¹, Jessica M. Lindsay⁶, Ajit Subramaniam¹, Kate E. Turner⁷, Alex
Whiting⁸

¹Lamont-Doherty Earth Observatory, Columbia University, Palisades, NY, USA, ²Geophysical
Institute, University of Alaska Fairbanks, Fairbanks, AK, USA, ³Community of Kotzebue,
Kotzebue, AK, USA, ⁴Farthest North Films, Homer, AK, USA, ⁵International Arctic Research
Center, University of Alaska Fairbanks, Fairbanks, AK, USA, ⁶University of Washington Seattle
Campus, Seattle, WA, USA, ⁷National Institute of Water and Atmospheric Research,
Wellington, New Zealand, ⁸Native Village of Kotzebue, Kotzebue, AK, USA

Corresponding author: Nathan Laxague (Nathan.Laxague@unh.edu)

†Current affiliation: Department of Mechanical Engineering and Center for Ocean Engineering,
University of New Hampshire, Durham, NH, USA

Key Points:

- High-resolution aerial radiometric observations were made over heavily-degraded first-year sea ice in Arctic Alaska.
- Large regions of blue-green ice were observed to be associated with strong net solar irradiance into the surface.
- Snowy ice features increased in reflectance with size up to a critical scale, with no size dependence beyond that.

23 **Abstract**

24 In polar regions, sea ice is a crucial mediator of the interaction between earth's atmosphere and
25 oceans. Its formation and breakup is intimately connected with local weather patterns and larger-
26 scale climatic processes. During the spring melt and breakup period, snow-covered ice transitions
27 to open water in a matter of weeks. This has a profound impact on the use of sea ice in coastal
28 Arctic regions by Indigenous People, where activities such as hunting and fishing are central to
29 community livelihood. In order to investigate the physical phenomena at the heart of this process,
30 a set of targeted, intensive observations were made over Spring sea ice melt and breakup in
31 Kotzebue Sound, Alaska. This program is part of the Ikaagvik Sikukun project, a collaborative
32 effort in which an Indigenous Elder advisory council from Kotzebue and scientists participated in
33 co-production of hypotheses and observational research, including a stronger understanding of the
34 physical properties of sea ice during spring melt. Data were collected using high-endurance, fixed-
35 wing uncrewed aerial vehicles (UAVs) containing custom-built scientific payloads. Here we
36 present the results of these measurements. Repeated flights over the measurement period captured
37 the early stages of the transition from a white, snow-covered state to a broken up, bare/blue-green
38 state. We found that the reflectivity of a surface type depends on the size and shape of the features
39 which constitute it. Specifically, large bare blue-green ice features were found to be least reflective,
40 while large snowy/white ice features were found to be most reflective.

41 **Plain Language Summary**

42 We performed a series of airborne observations aimed at describing the types and sizes of features
43 that are most strongly connected to the absorption of solar energy. We found that feature size and
44 shape affects the tendency of sea ice to absorb solar energy and melt. Specifically, we found that
45 large patches of bare blue-green ice are the most strongly absorptive, and that as regions of snowy
46 white ice become smaller, they become less reflective.

47 **1 Introduction**

48 Sea ice is an essential feature of the polar oceans, looming large as both visual wonder and
49 geophysical presence. The standard processes of air-sea interaction---whereby fluxes of
50 momentum, heat, and mass are mediated by turbulent flow past an undulating interface---are
51 fundamentally transformed by the presence of sea ice which attenuates (or completely suppresses)
52 surface waves and wind-forced currents. However, there is perhaps no sea ice-related geophysical
53 effect more stark than its alteration of the solar radiative balance. Whereas the ice-free ocean tends
54 to reflect less than 10% of incoming solar radiation, the myriad forms of snow and ice at various
55 stages of melt and degradation will reflect between 15-90% of incoming solar radiation.
56 Broadband albedo, the ratio of wavelength-integrated reflected solar irradiance to incident solar
57 irradiance, is strongly dependent on the surface state of the ice (Perovich et al., 1998), with
58 fractional cover of snow on the surface the single most important determinant of high albedo
59 (Yackel et al., 2000). The formation of melt ponds on the surface of sea ice alters surface radiative
60 properties, lowering surface albedo (Barber & Yackel, 2010) and increasing the transmittance of
61 light through the ice into the underlying sea (Ehn et al., 2011; Frey et al., 2011; Light et al., 2015).
62 It has long been known that solar radiative heat flux into the sea ice surface contributes to melting,
63 reducing its reflectance and increasing its susceptibility to further degradation (Budyko, 1969).
64 This phenomenon, known as the ice-albedo feedback, is understood to be a key component of the
65 Earth's climatic variability. The rapid decline in sea ice extent in the recent past (Brennan et al.,

2020) has led to an aggregate scale change in surface albedo as ice melts completely and is replaced by open water. Additionally, a widespread decline in Arctic sea ice thickness has been observed over the past half-century (Kwok & Rothrock, 2009). This is largely due to another feedback: as sea ice thins, it reflects less solar radiation (Lu et al., 2016) and allows for greater transmission of light (Light et al., 2008). This in turn results in increased ocean heat and enhanced melting of the sea ice bottom (Planck et al., 2020).

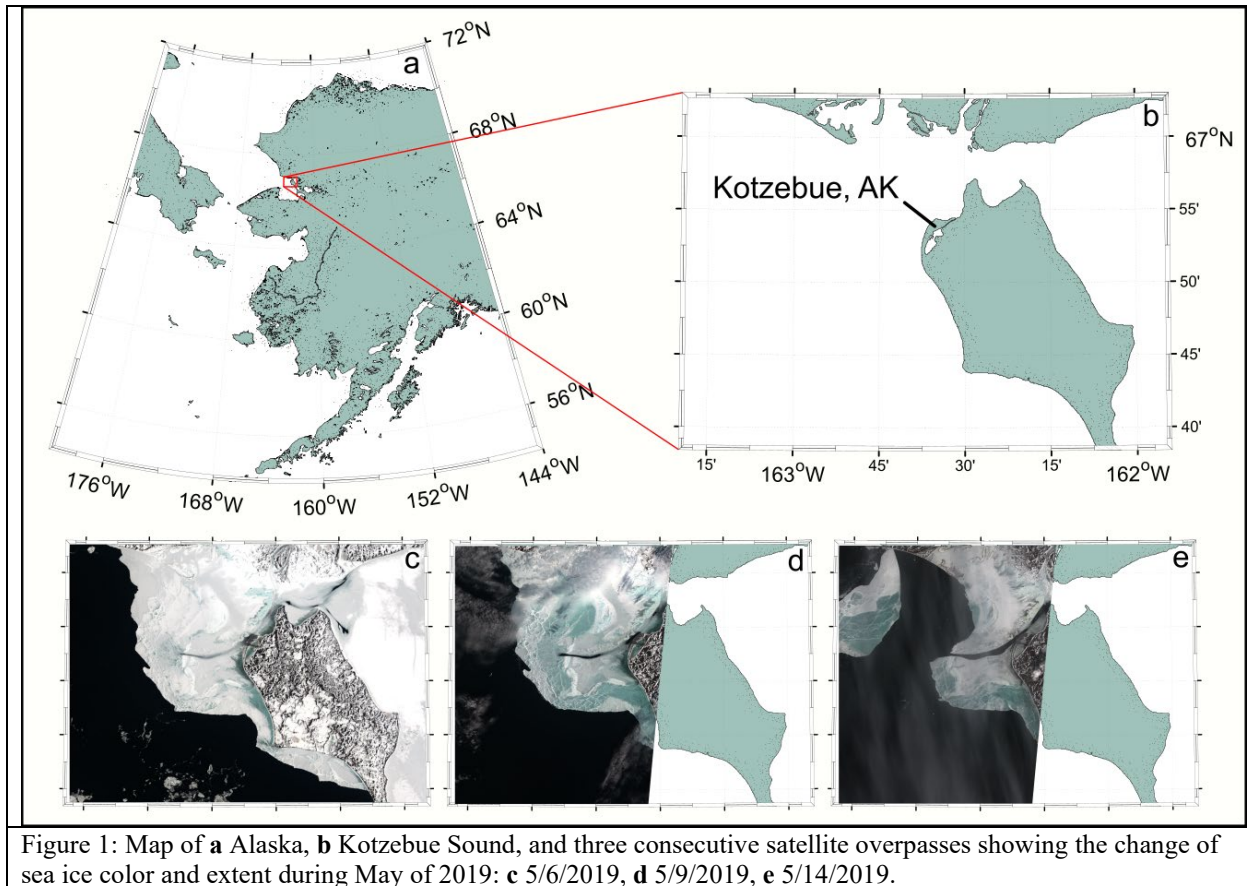


Figure 1: Map of **a** Alaska, **b** Kotzebue Sound, and three consecutive satellite overpasses showing the change of sea ice color and extent during May of 2019: **c** 5/6/2019, **d** 5/9/2019, **e** 5/14/2019.

Recent changes to the thickness, surface state, and overall extent of sea ice have yielded a dramatic increase in the absorption of solar heat in the Arctic Ocean (Perovich & Polashenski, 2012). This has resulted in the Arctic warming at nearly four times the global average rate (Rantanen et al., 2022), a phenomenon named Arctic amplification. There is abundant evidence that this is due to the diminishment of sea ice cover and thickness (Dai et al., 2019; Perovich et al., 2020; Screen & Simmonds, 2010). All of these trends have led to the Arctic system becoming far less resilient to change than it was decades ago (Overland, 2020). The consequences of these effects are most concrete, immediate, and stark for Indigenous Arctic communities who exist among the sea ice and often rely upon it as part of their way of life (Gearheard et al., 2013). For decades, the melt season has been trending to occur sooner and last for longer each year (Markus et al., 2009; Stroeve et al., 2014), threatening long-practiced Indigenous traditions such as seasonal hunts (Hauser et al., 2021).

In order to improve our understanding of the processes which drive these changes, there is a need for new field observations which quantify surface fluxes in high-latitude environments (Bourassa

86 et al., 2013). So-called ‘process’ studies which target particular physical phenomena are
 87 particularly illuminating (Carmack et al., 2015). When conducting research on adaptation to
 88 climate change, it is valuable to move from an extractive (David-Chavez & Gavin, 2018)
 89 framework to one of co-production and stakeholder engagement (Klenk et al., 2017). The co-
 90 production of knowledge with local research partners is at its most effective when it is both
 91 iterative and interactive (Bremer et al., 2019), incorporating the needs of the community with an
 92 understanding of global-scale challenges (Eicken et al., 2021). This shift in mindset benefits the
 93 local communities most directly impacted by the processes being studied- but it also benefits the
 94 scientific research itself, with Indigenous Knowledge-holders providing key insights into local
 95 dynamics (Eicken, 2010), especially when equity between Indigenous People and scientists is a
 96 key component of the co-production framework (Yua et al., 2022).

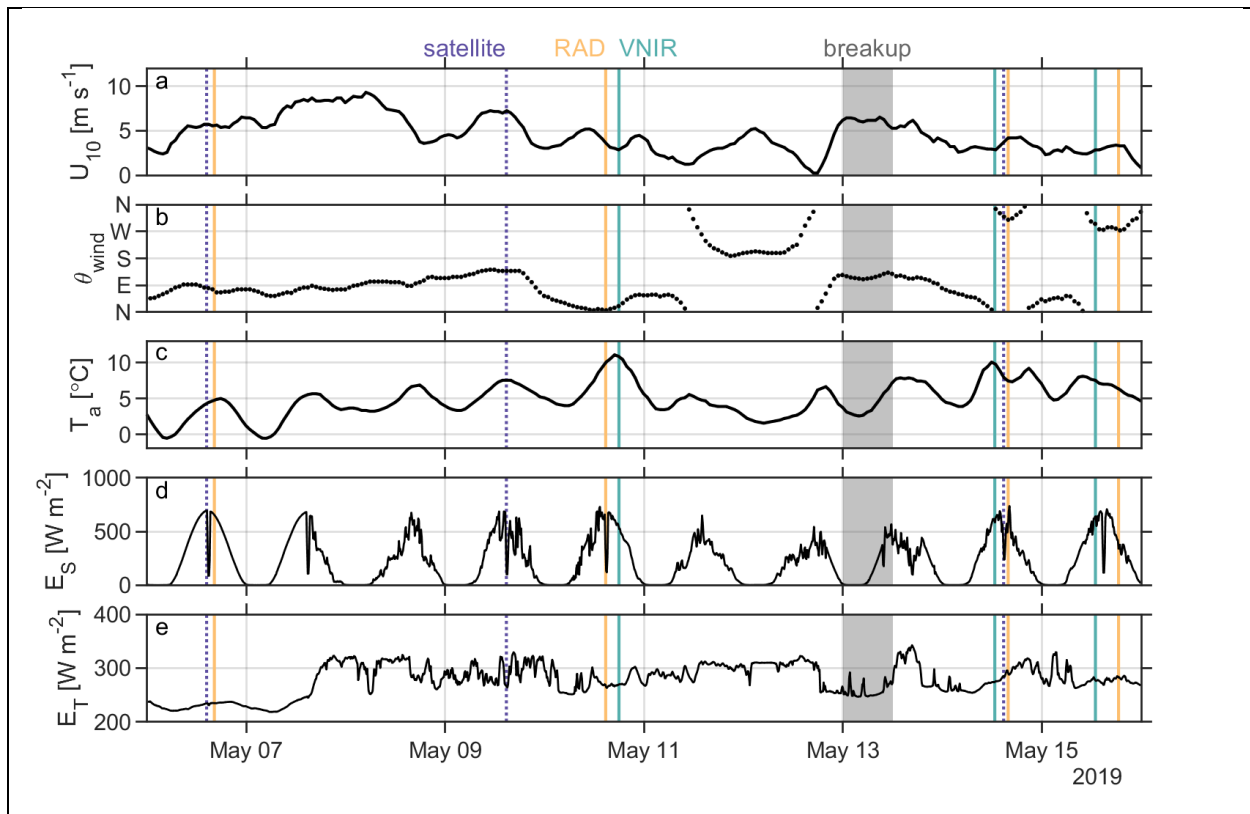
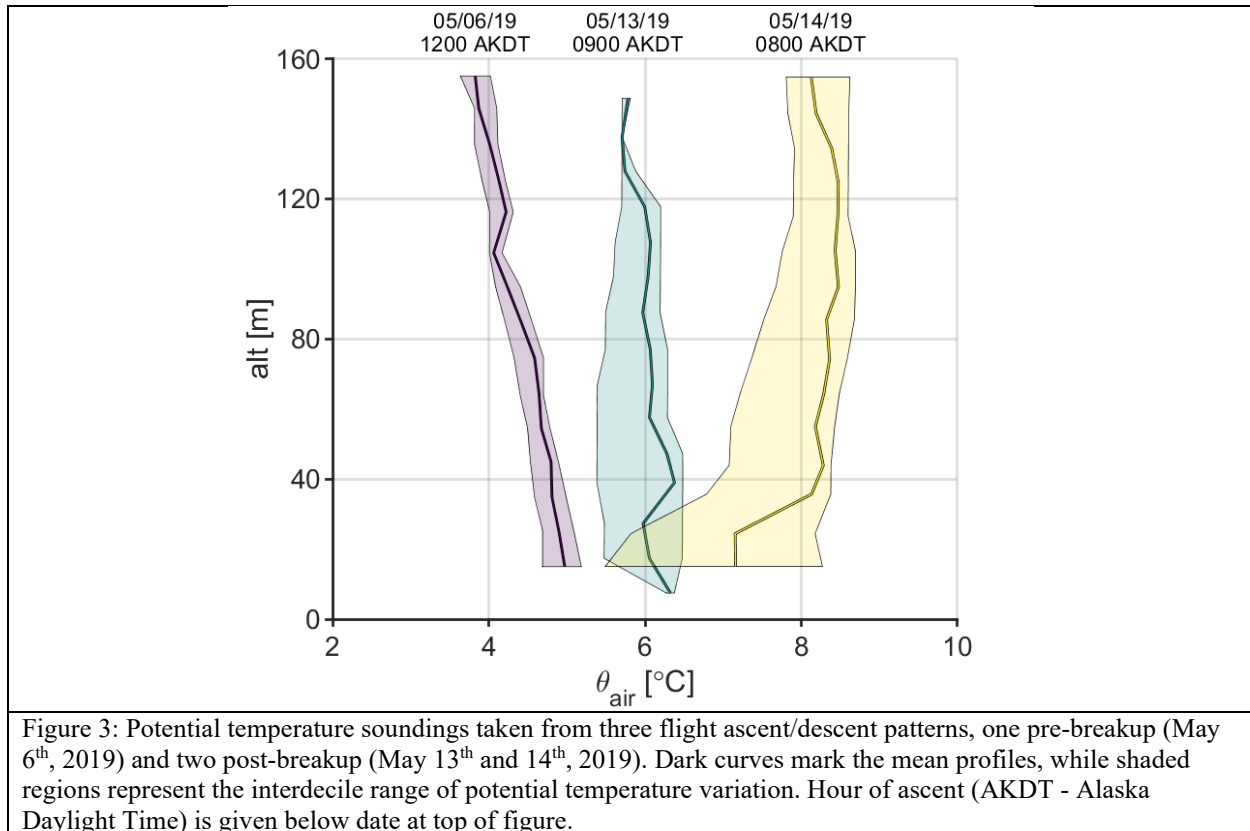


Figure 2: Environmental conditions during field campaign: **a** wind speed, **b** wind direction (coming-from convention), **c** air temperature, **d** downwelling solar irradiance, and **e** downwelling thermal irradiance. Wind/air measurements were made at Kotzebue Ralph Wien Airport, while radiative measurements were made at the U.S. Fish & Wildlife Service bunkhouse. Vertical lines indicate times of satellite overpasses (dotted violet), UAV flights with “RAD” payload (solid orange), UAV flights with “VNIR” payload (solid teal); gray shaded region denotes approximate time of major sea ice breakup.

97 The present study arose as part of the Ikaagvik Sikukun project, a collaborative effort of knowledge
 98 co-production and observational research completed by an Indigenous Elder advisory council
 99 (study co-authors J.G., C.H., R.J.S., and R.S., Sr.) from Kotzebue, AK (Figure 1) and an
 100 interdisciplinary team of scientists. This project was community-involved from the outset, with
 101 the initial stage of collaboration centered around the generation of driving research questions
 102 largely focused on understanding the physical and biological changes associated with sea ice loss
 103 in Kotzebue Sound (Hauser et al., 2021; Lindsay et al., 2023; Mahoney et al., 2021; Witte et al.,

104 2021). In many coastal regions, the onset of sea ice breakup is associated with a seasonal hunting
 105 period; in Kotzebue Sound, the Qikiqtagruṃmiut hunt of *ugruk* (bearded seal) coincides with the
 106 breakup of sea ice. The details of this connection—and of our co-production of knowledge
 107 approach—is described in more detail by (Hauser et al., 2021). These factors were to be
 108 investigated using a variety of in situ, satellite, and uncrewed airborne observations. It is the latter
 109 set of high-resolution observations made from a series of flights throughout a period of advanced
 110 melt that form the basis of the present study.



111 Satellite images of Kotzebue Sound taken during our field observational campaign (Figure 1) show
 112 that the region’s landfast sea ice appeared mostly blue-green by 5/9, with a major breakup event
 113 occurring between 5/13 and 5/14. Several important physical parameters are shown as stacked
 114 timeseries in Figure 2, with vertical lines indicating the timing of satellite overpasses and UAV
 115 flights (with the “RAD” and “VNIR” payloads, to be defined in section 2). These were obtained
 116 from land-based instrumentation: air temperature and wind velocity data from the meteorological
 117 station at Kotzebue Ralph Wien Airport (station PAOT); downwelling hemispheric radiative
 118 fluxes from a pair of Kipp & Zonen sensors (pyranometer and pyrgeometer) mounted on the
 119 rooftop of the U.S. Fish and Wildlife office. For the majority of our observational period, the sky
 120 was quite cloudy- this can be seen in the downwelling radiative flux time series of Figure 2, with
 121 high thermal irradiance and spottiness in solar irradiance (that is, departure from its characteristic
 122 bell-shaped diurnal behavior). The major landfast ice breakup event (indicated by the gray shaded
 123 region on Figure 2) was preceded by a rapid transition in the wind forcing, with onshore wind of

124 5 m/s giving way to offshore wind of 7 m/s. This transition in atmospheric conditions extended
125 well into the atmospheric boundary layer (Figure 3).

126 2 Methods

127 2.1 UAV-based radiometry

128 For this work, we deployed uncrewed aerial vehicles (UAVs) equipped with specialized payloads
129 for sensing downwelling (sky-leaving) and upwelling (surface-leaving) radiative fluxes in
130 solar/shortwave and thermal/longwave bands. These sensors are listed below in table 1.

Quantity	Dimensions	Symbol	Sensor	Payload & Orientation	Spectral Sensitivity	Surface Spatial Resolution
Thermal irradiance	W/m^2	E_T	Hukseflux IR02 Pyradiometer	RAD, up & down	4.5 – 40 μm	N/A
Solar irradiance	W/m^2	E_s	Hukseflux SR03 Pyranometer	RAD, up & down	285 – 3000 nm	N/A
Solar spectral irradiance	$W/m^2/nm$	$E_s(\lambda)$	OceanOptics USB2000 Irradiance Spectrometer	VNIR, up	200 – 1100 nm	N/A
Solar spectral radiance	$W/m^2/nm/sr$	$L_s(\lambda)$	Headwall Micro-HyperSpec VNIR A-Series Imaging Spectrometer	VNIR, down	400 – 1000 nm	57 cm @ 1000 m altitude

131
132 Table 1: Inventory of radiative measurements made via UAV, including the spectral sensitivity and surface spatial
133 resolution.

134 The details of the UAS deployed during our field operations are provided by (Zappa et al., 2020);
135 what follows here is a summary of the elements most relevant to the present study. Each UAV
136 carried in its nosecone a “Base” payload (holding the core power and data management systems)
137 and one of a number of modular payloads which allowed for specialized sensor deployment. The
138 RAD and VNIR payloads were deployed for observing the radiative properties of the sea ice; their
139 core onboard sensors are listed in table 1. The RAD payload contained up and down-looking
140 Hukseflux model IR-02 pyrgeometers to measure thermal irradiance and up and down-looking
141 Hukseflux model SR-03 pyranometers to measure solar irradiance, all sampled at 1 Hz. The VNIR
142 payload contained an upward-looking Ocean Optics model USB2000+ spectrometer to measure
143 downwelling visible and near-infrared spectral irradiance and a downward-looking Headwall
144 Micro-Hyperspec imaging spectrometer to measure upwelling visible and near-infrared spectral
145 radiance, all sampled at 25 Hz. The Headwall imaging spectrometer is a ‘pushbroom’ sensor, with
146 each image ‘frame’ corresponding to 1004 cross-track pixels (at 0.032° IFOV) and 1004 spectral
147 wavelengths (at 1.85 nm spectral resolution); of the 1004 spectral measurements, 216 fell within
148 the wavelength range of 400-800 nm used for the analysis here. Each UAV’s Base payload held
149 an onboard inertial navigation unit (INU) comprised of a GPS receiver and an inertial measurement
150 unit (IMU); a complementary ground station allowed for differential GPS post-processing. After
151 each flight, all GPS and IMU data were combined via tightly-coupled processing, providing an

152 integrated TSPI (time space position information) solution with centimeter-scale (± 1 cm
 153 horizontal, ± 2 cm vertical) position accuracy and 0.01° attitude accuracy.

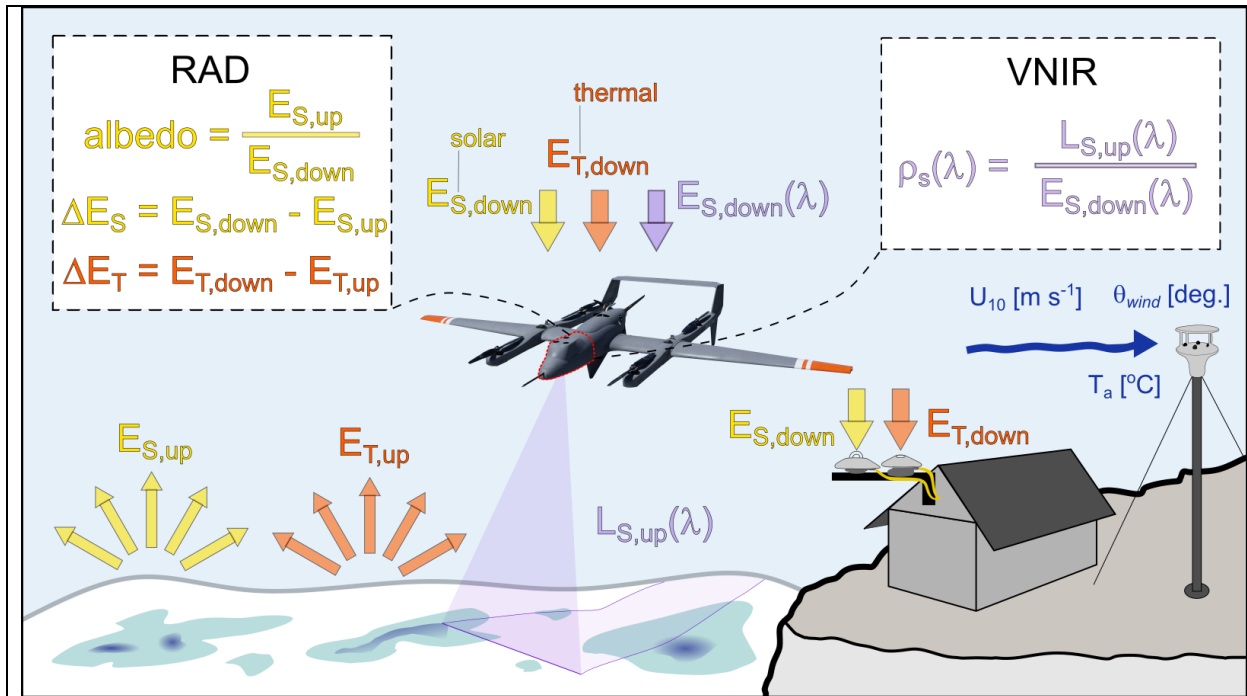
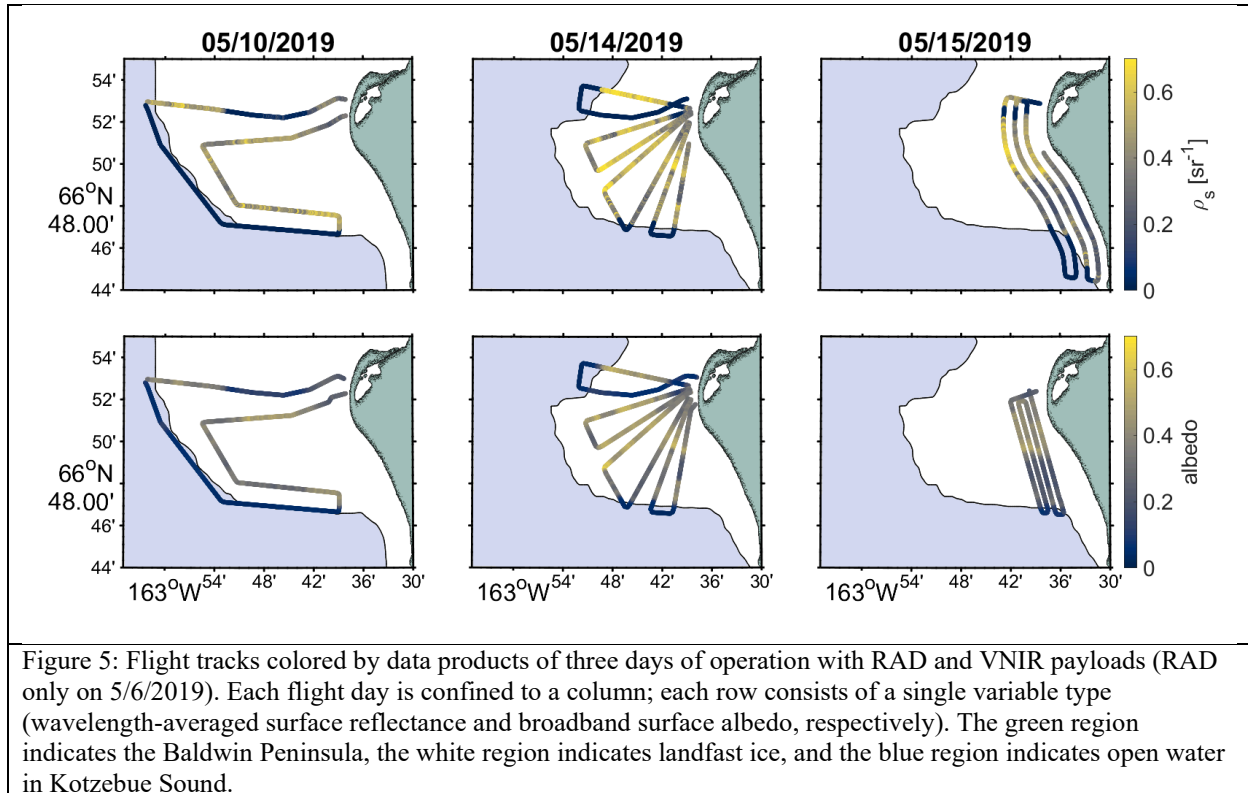


Figure 4: Depiction of fixed and aerial observational platforms, with arrows indicating radiative fluxes. Red dashed region on UAV indicates modular nosecone, with two red dashed boxes showing the measurement capabilities of two payloads: “RAD” payload, with upward/downward-looking pyranometers and pyrgeometers for characterizing upwelling and downwelling thermal and solar radiative fluxes; “VNIR” payload, with a downward-looking hyperspectral pushbroom imager and upward/downward-looking spectrometers for characterizing the spectral surface reflectance. Downwelling thermal and solar radiative fluxes were also measured from a rooftop station at the U.S. Fish and Wildlife Service bunkhouse. Wind speed, direction, and air temperature were measured from a meteorological station at Kotzebue Ralph Wien Airport.

154 It has been standard practice to separate sea ice features into distinct categories (e.g., snow, bare
 155 ice, melt ponds) and measure spectral albedo over those regions (Grenfell & Perovich, 1984, 2004;
 156 Perovich, Grenfell, et al., 2002). The relatively high altitude of our measurements rendered the
 157 hemispheric observations of the RAD payload too coarse to parse the radiative signatures of
 158 individual feature types. Given an altitude of 150 m, and the assumption that our hemispheric
 159 radiometers are ideal cosine collectors, we estimate that 90% of the signal originates from a region
 160 below the aircraft with diameter of 270 m. In order to complement these observations, VNIR
 161 payload performed measurements of sea ice spectral radiance, allowing for discernment of
 162 radiative characteristics at decimeter-scale spatial resolution.

163 The irradiance data obtained via sensors on the RAD payload were used to compute net solar
 164 irradiance, net thermal irradiance, and shortwave albedo (Figure 4). The downwelling spectral
 165 irradiance and upwelling spectral radiance data obtained via sensors on the VNIR payload were
 166 used to compute the spectral surface reflectance (Figure 4). The mean surface VNIR reflectance
 167 and broadband albedo observed along the track of each of the UAV flights are shown in Figure 5.
 168 Note that the surface reflectance measurements are localized in space (no more than 250 meters
 169 on either side of the flight track) while the albedo measurements were obtained via hemispheric
 170 sensors, integrating information from a far broader spatial region. Care was taken to ensure that

171 ambient radiative conditions did not differ too greatly from one flight to the next. As shown in the
 172 time series of Figure 2, the incoming irradiance did not vary greatly across the VNIR flights ($E_S =$
 173 $570 \pm 50 \text{ W m}^{-2}$, $E_T = 275 \pm 5 \text{ W m}^{-2}$). The disparate tracks from one flight day to the next resulted
 174 from rapidly-changing surface conditions; for the first two sets of flights, RAD and VNIR payloads
 175 followed the same flight paths. However, by 5/15, the degradation of the sea ice surface advanced
 176 to the point that our visual observer could not maintain line of sight with the aircraft, resulting in
 177 different flight plans for the RAD and VNIR payloads on that day.



178 2.2 Sea ice surface feature identification and processing

179 Surface reflectance data obtained from the VNIR payload were georeferenced according to the
 180 aircraft's attitude and position from the tightly-coupled TSPI solution. At a flight altitude of 1000
 181 m, the total position error of each georeferenced radiance observation was estimated to be <20 cm,
 182 smaller than the 57 cm ground sample distance (table 1). The 'pushbroom' processing is most
 183 readily described visually; please see appendix Figure A1 for a step-by-step view of the
 184 georeferencing.

185 The calibrated surface reflectance maps were bin-averaged in wavelength space with a spectral
 186 width of 5 nm; this provided an improvement to signal-to-noise ratio, especially for measurements
 187 in the violet and near-infrared ranges. Given that our principal interest lay in fixed features on sea
 188 ice, the next major step taken was to exclude regions of open water; these were identified as regions
 189 for which the mean spectral reflectance was less than 0.05. There is a wide range of surface

190 classification schemes available given imagery of the sea ice surface-- even RGB or panchromatic
 191 imagery (Wright & Polashenski, 2018).

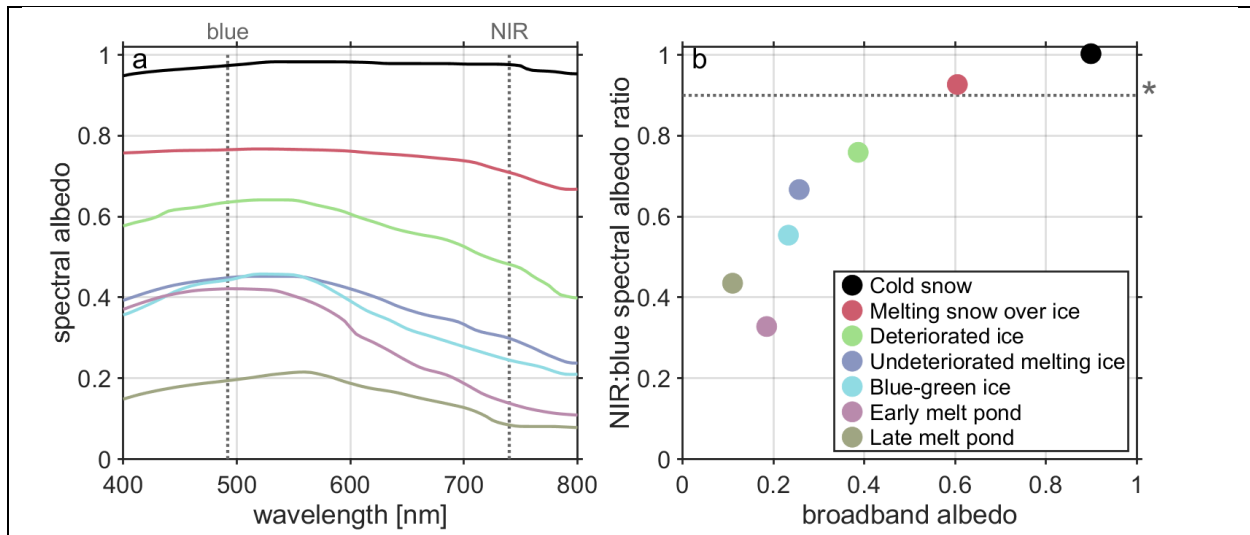


Figure 6: Spectral albedo (a) and the ratio between the spectral albedo in the near-infrared (NIR) and blue, or NIR:B (b) for a variety of classifications of first-year sea ice, organized by broadband albedo. Data shown in (a) were taken from (Perovich, 2017) and used to compute quantity shown in (b). Asterisk in panel (b) indicates a NIR:blue ratio of 0.9.

192 Given our hyperspectral visible and near-infrared observations of the surface, we are able to
 193 perform classification based on surface radiative properties. The approach chosen here was
 194 informed by the surface-dependent spectral albedo measurements of (Perovich, 2017) shown in
 195 Figure 6a. The ratio between surface reflectance in the near-infrared (740 ± 10 nm) and blue
 196 (490 ± 10 nm) visualized in Figure 6b- hereafter “NIR:B”- provides a reasonable separation point
 197 between spectrally flat (NIR:B~1) features of sea ice often characterized by snow cover and the
 198 blue/green features associated with a more advanced stage of melt (NIR:B<1). A demonstration
 199 of this partitioning is provided in Figure 7.

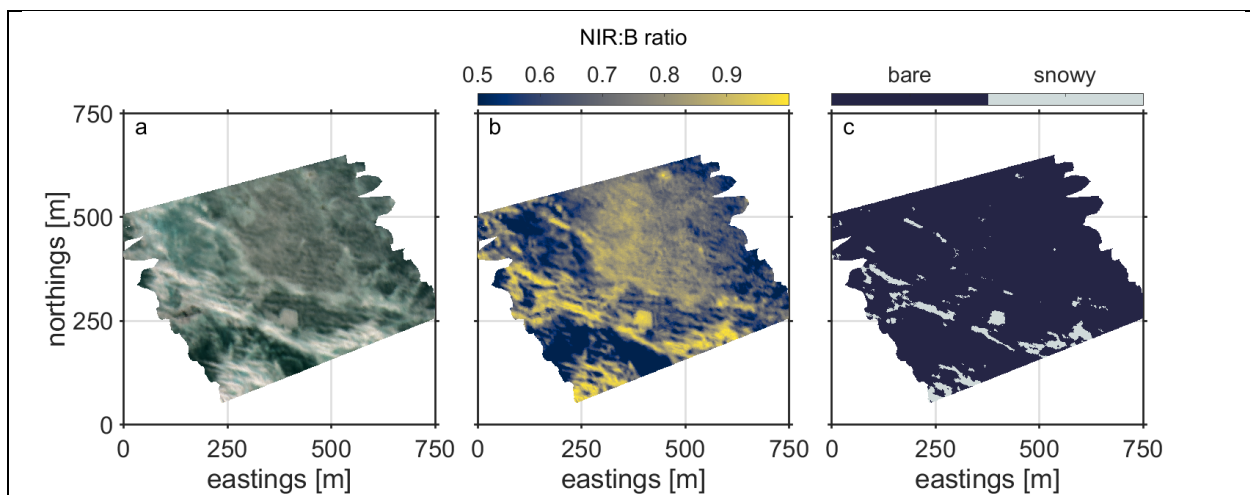


Figure 7: (a) Color mosaic produced from the red, green, and blue channels of ρ_s . (b) Ratio of the NIR and blue channels of ρ_s , (NIR:B). (c) Binarized frame showing separation into ‘bare’ and ‘snowy’ portions.

200 As indicated by Figure 6, partitioning the surface at a NIR:B value of 0.9 will bundle together bare
 201 ice with ponded ice. A second step of separation is required in order to parse melt ponds from the
 202 bare ice regions identified via the NIR:B approach. For this, we turned to the technique of (König
 203 & Oppelt, 2020), whereby the *slope* of the spectral reflectance in the near-infrared may be
 204 interpreted to infer the melt pond depth. The combined two-layer processing involves a check for
 205 melt ponds (which are then excluded from further partitioning) followed by a thresholding along
 206 the NIR:B value of 0.9. A demonstration of this processing is shown in Figure 8.

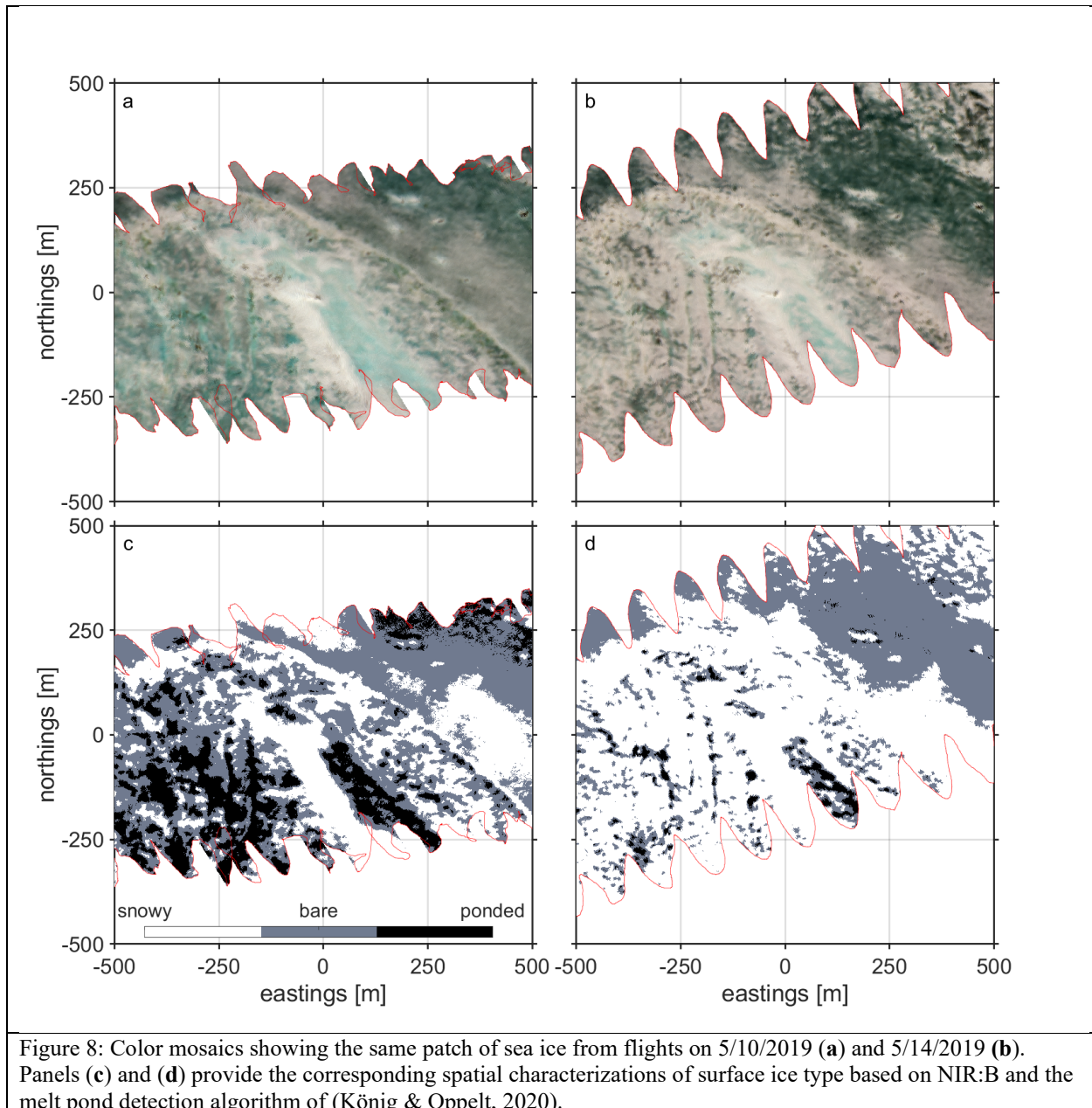


Figure 8: Color mosaics showing the same patch of sea ice from flights on 5/10/2019 (a) and 5/14/2019 (b). Panels (c) and (d) provide the corresponding spatial characterizations of surface ice type based on NIR:B and the melt pond detection algorithm of (König & Oppelt, 2020).

207 This scheme yields a three-level classification, allowing for statistical analysis to be performed on
 208 the geometric and radiative characteristics of ponded, bare, and snowy ice features ranging from
 209 decimeters to hundreds of meters in length scale. MATLAB's *regionprops* function was used for
 210 this processing, yielding the area and perimeter of each detected feature as well as the spectral

211 surface reflectance at each point within each feature. Regions smaller than nine pixels (area < 2.4
 212 m^2) were excluded in order to ensure that feature geometry was not over-constrained by the
 213 discretization. Regions larger than $100,000 \text{ m}^2$ were also excluded in order to neglect cases for
 214 which the entire field of view was filled with a particular surface type. It is often convenient to
 215 reduce the width of the parameter space by representing features in terms of characteristic length
 216 scale “ D ” rather than area. Given only the feature area, this may be done via simple square root,
 217 assuming the patch is a square: $D = \sqrt{\text{area}}$; more realistically, as the diameter of a circle with that
 218 area: $D = \sqrt{4/\pi \text{ area}}$. Given both the feature area and the feature perimeter, one may compute
 219 the characteristic length scale $D = \frac{4 \cdot \text{area}}{\text{perimeter}}$; for a circular feature, D becomes the diameter.

220 3 Results

221 3.1 Spatially-averaged properties

222 By combining the observations from consecutive RAD-VNIR flights, it is possible to relate the
 223 surface spectral reflectance (and color) to the net solar irradiance. This is shown in Figure 9, with
 224 mean visible and near-infrared surface reflectance plotted against net solar irradiance in Figure
 225 9a and the spectral surface reflectance binned by net solar irradiance in Figure 9b. Marker color
 226 in Figure 9a was generated from the reflectance in the red, green, and blue bands. Spectrally-flat
 227 surfaces (appearing white or gray) are associated with lower net solar irradiance; surfaces
 228 colored blue-green are associated with higher net solar irradiance. This is borne out in the binned
 229 spectra of Figure 9b, with higher net solar irradiance occurring for lower surface reflectance- but
 230 especially lower surface reflectance in the red and near-infrared regimes.

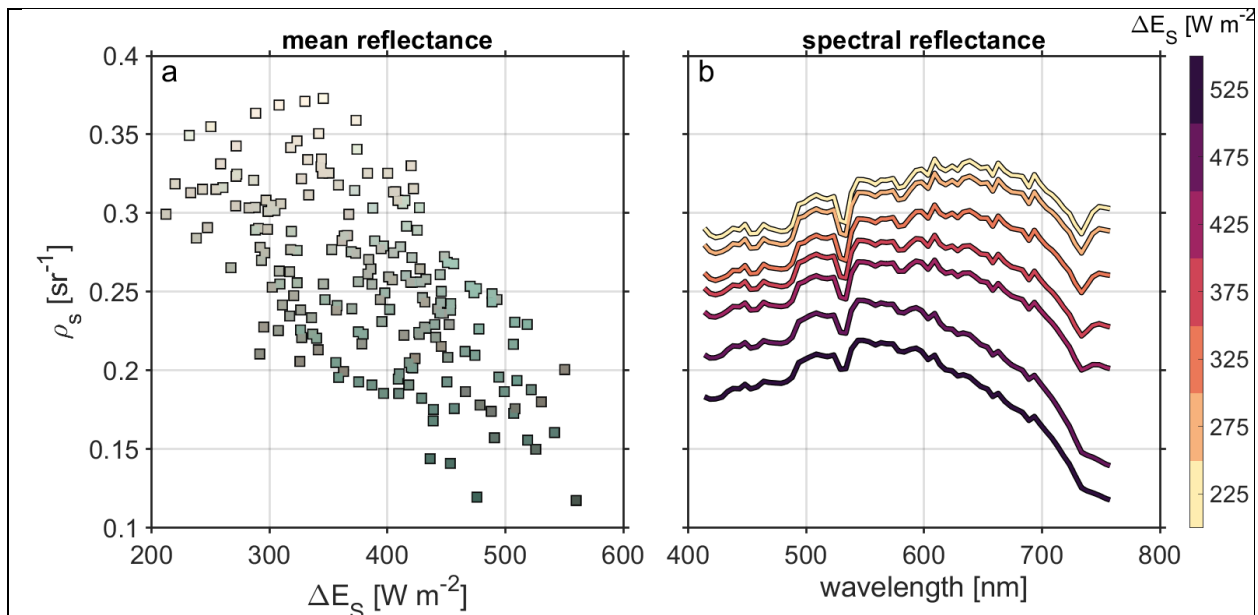


Figure 9: **a** Spatially-averaged surface reflectance ρ_s as a function of net solar irradiance. Marker color corresponds to the surface color determined by the red, green, and blue channels of ρ_s . **b** Spatially-averaged spectral surface reflectance $\rho_s(\lambda)$, with color indicating the bin-averaged net solar irradiance.

231 3.2 Geometric properties of surface features

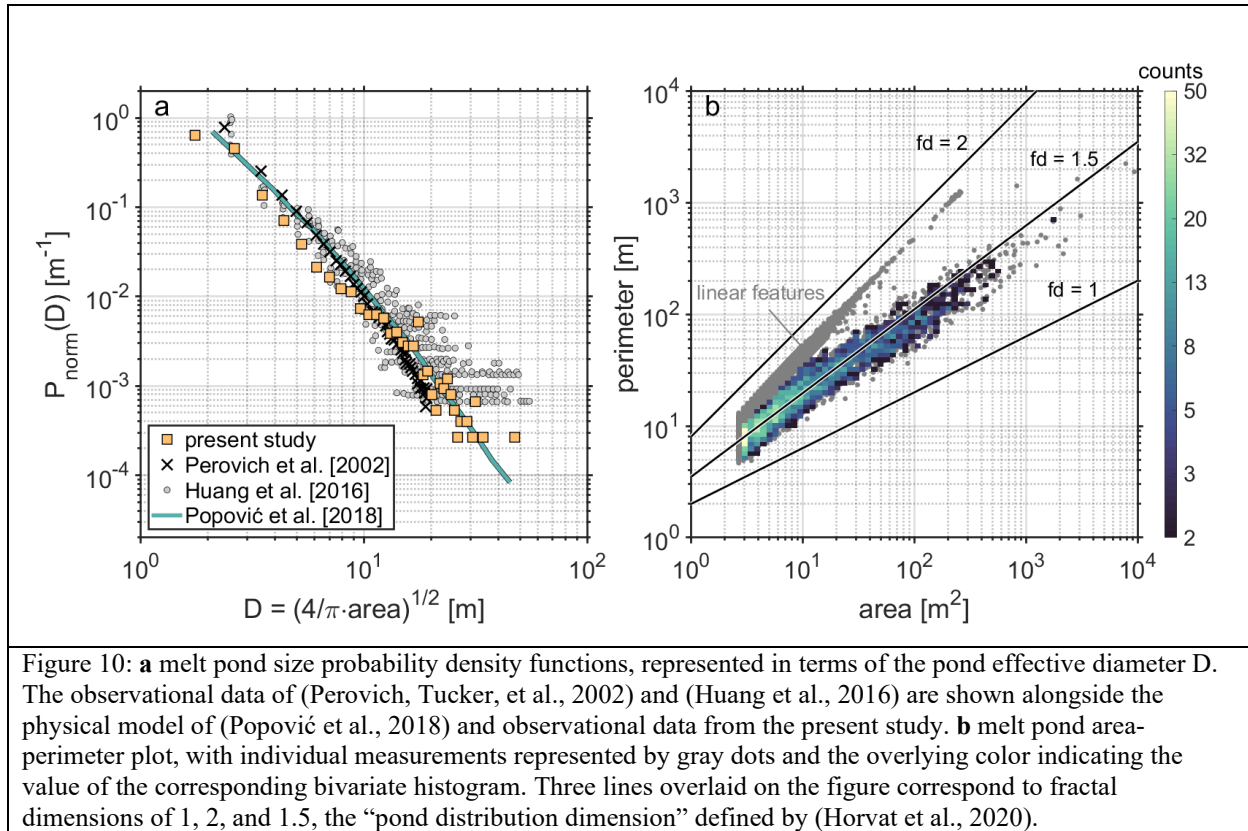


Figure 10: **a** melt pond size probability density functions, represented in terms of the pond effective diameter D . The observational data of (Perovich, Tucker, et al., 2002) and (Huang et al., 2016) are shown alongside the physical model of (Popović et al., 2018) and observational data from the present study. **b** melt pond area-perimeter plot, with individual measurements represented by gray dots and the overlying color indicating the value of the corresponding bivariate histogram. Three lines overlaid on the figure correspond to fractal dimensions of 1, 2, and 1.5, the “pond distribution dimension” defined by (Horvat et al., 2020).

232 The bulk of section 2.2 was devoted to describing a framework for sea ice feature classification
 233 and geometric/radiative analysis. We now show the results of employing that framework. The
 234 relationship between area and perimeter offers more than a convenient way of rendering feature
 235 length scale- it provides us with information about the fractal dimensionality of the features on the
 236 sea ice surface. One such approach for determining fractal dimension (here given as fd rather than
 237 the literature-standard D in order to avoid confusion with our length scale D) is the aptly-named
 238 area/perimeter relationship (Klinkenberg, 1994): $P \propto (\sqrt{\text{area}})^{fd}$. In practical terms, fd is
 239 computed as half the slope of the relationship between $\log(\text{perimeter})$ and $\log(\text{area})$; this
 240 approach has been applied to melt pond data produced from observations (Hohenegger et al., 2012)
 241 and physical geometric modeling (Bowen et al., 2018; Horvat et al., 2020). A value of $fd = 1$
 242 indicates that perimeter scales as the square root of the area (true for non-overlapping simple
 243 shapes). In mathematical terms, $fd = 2$ represents a shape-filling curve; in our practical application,
 244 fd approaching 2 represents linear features that are one ground sample distance wide.

245 The size distribution and area/perimeter relationship of surface melt ponds are provided in Figure
 246 10; panel a also includes the melt pond size distributions produced from the aerial field
 247 observations of (Perovich, Tucker, et al., 2002) and (Huang et al., 2016) and the geometric ‘void’
 248 model of (Popović et al., 2018), all represented in terms of characteristic length scale $D =$
 249 $\sqrt{4/\pi \text{ area}}$. The area/perimeter relationship in panel b is represented with a cloud of gray points
 250 indicating individual measurements overlaid with a bivariate histogram that excludes the ‘linear

251 features' which bump up against the sensor spatial resolution. The melt pond area/perimeter
 252 relationship has been shown to reveal a sigmoid transition in fractal dimension from 1 to 2, with
 253 the inflection point tending to occur around a feature area of 100 m² (Hohenegger et al., 2012).
 254 Our observations do not show this relationship, likely due to the relative paucity of melt pond
 255 observations during our field campaign- less than 0.5% of the imaged sea ice surface area
 256 contained ponded ice. Indeed, the mean fractal dimension (or, as in (Horvat et al., 2020), 'pond
 257 distribution dimension) of ~1.5 appears to indicate that a large fraction of the detected melt ponds
 258 had a small area.

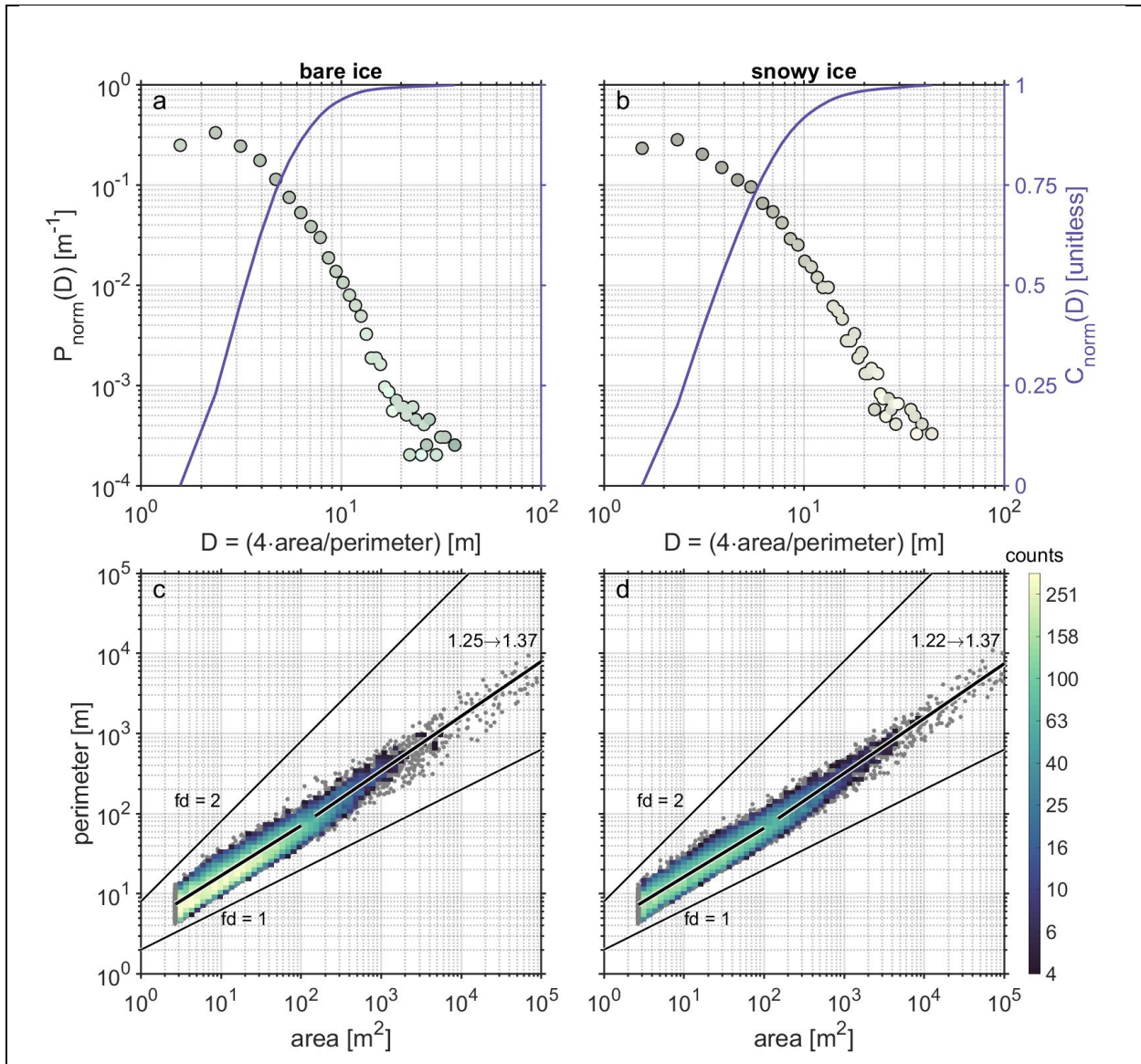
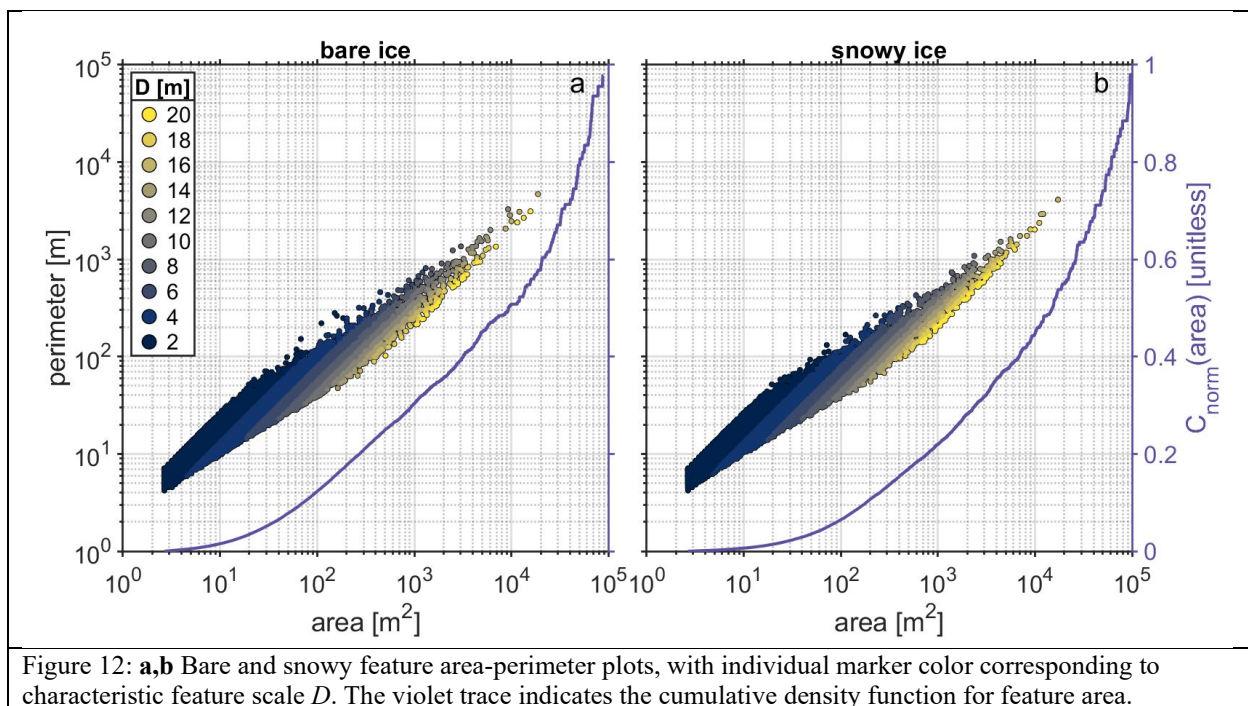


Figure 11: Probability density functions describing snowy ice feature geometry; the layout is generally analogous to that of Figure 10: **a,b** bare and snowy ice feature size probability & cumulative density functions, represented in terms of the pond effective diameter D . Marker color corresponds to the mean feature color for a particular size bin. **c,d** bare and snowy feature area-perimeter plots, with individual measurements represented by gray dots and the overlying color indicating the value of the corresponding bivariate histogram. Two lines overlaid on the figures correspond to fractal dimensions of 1 and 2; the piecewise linear functions correspond to fractal dimensions computed over two regimes: areas ranging from 2.6 m² – 100 m² and 150 m² – 100,000 m².

259 The remaining 99.5% of sea ice surface that was not ponded therefore fell into our two other
 260 categories: bare and snowy. The multipanel Figure 11 contains size probability density functions
 261 and area/perimeter relationships for bare and snowy ice features. In panels (a-b), we show feature
 262 size distributions in terms of characteristic length scale $D = \frac{4 \cdot \text{area}}{\text{perimeter}}$. There appear to be two
 263 regimes in these distributions, with the probability density of large bare or snowy features falling
 264 off more steeply with diameter than that of the smaller, darker features. This transition may be
 265 analogous to the transition found for melt pond size distributions (Hohenegger et al., 2012;
 266 Popović et al., 2018) that follows the sharp increase in fractal dimension as a result of increasing
 267 melt pond complexity and connectedness. The geometric bivariate distributions shown in panels
 268 (c-d) provide a clearer picture of this transition. For both bare and snowy features, regions
 269 smaller than 100 m^2 have fractal dimension fd around 1.25 while features larger than 150 m^2
 270 have fd around 1.37.



271 Although small features dominate the size probability density functions- 99.5% of all bare ice
 272 features and 98.5% of all snowy ice features have $D < 20 \text{ m}$ - the majority of the surface is covered
 273 by large features. This can be seen in Figure 12; for bare ice, features with characteristic length

274 scale $D < 20$ m occupy only 44% of the total imaged surface. For snowy ice, the same scale range
 275 represents only 35% of the total imaged surface.

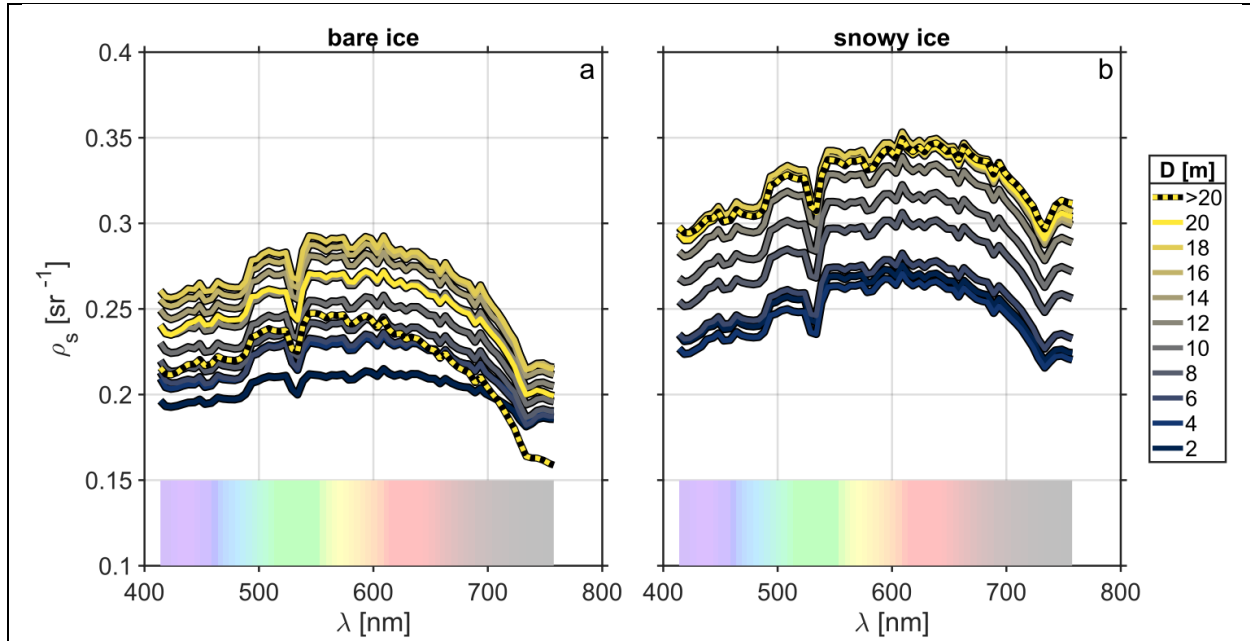


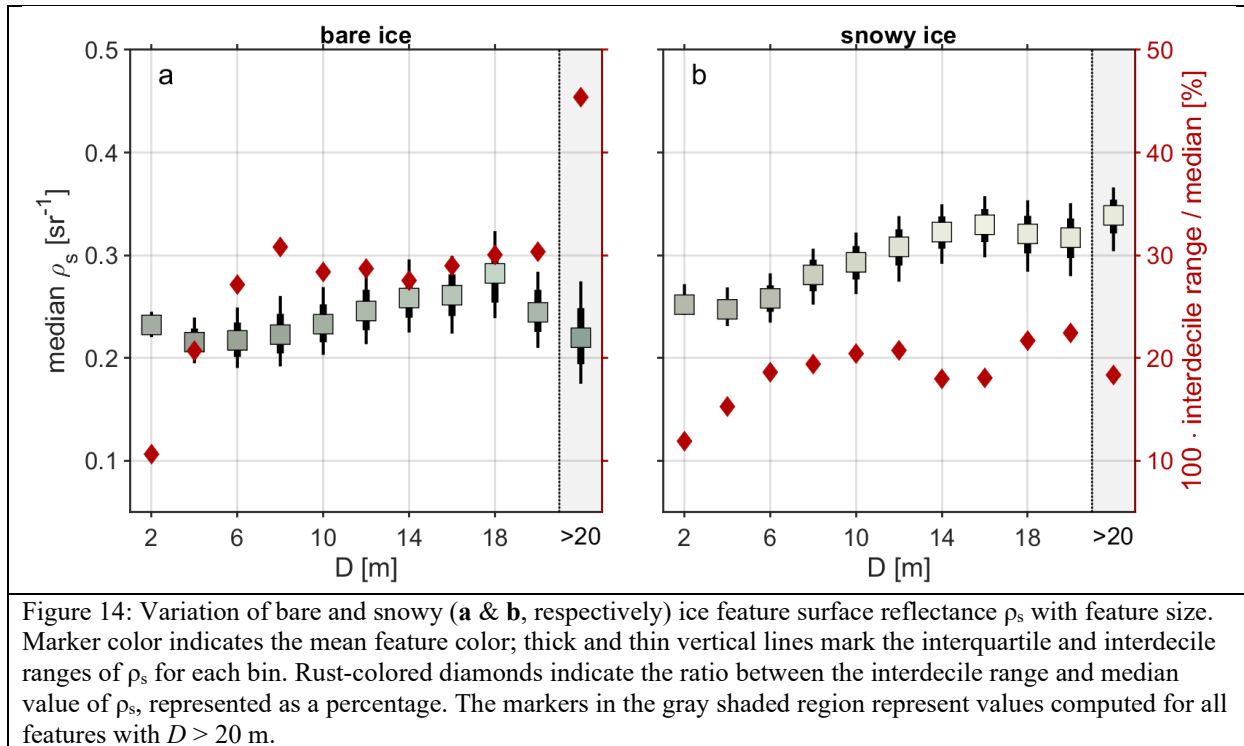
Figure 13: Surface reflectance spectra $\rho_s(\lambda)$ for bare and snowy ice (left and right panels, respectively). The thickness of each trace corresponds to the mean effective feature diameter D for which the spectra were bin-averaged. The dotted trace corresponds to the average for $D > 20$ m. The translucent rainbow bar at the base of the plot indicates the approximate color corresponding to each particular wavelength.

276 From the spatially-averaged reflectance and irradiance shown in Figure 9, we have arrived at the
 277 intuitive result that snowy surfaces are of higher total reflectance than bare surfaces-- and that
 278 red/near-infrared reflectance is particularly lower for bare ice. Our geometric analysis provides us
 279 with the ability to parse this effect by feature size. Figure 13 shows the surface reflectance spectra
 280 partitioned by surface type (bare and snowy) and characteristic length scale $D = \sqrt{\frac{4 \cdot \text{area}}{\text{perimeter}}}$ in
 281 bins separated by 2 m (± 0.5 m binwidth). The dotted yellow trace indicated by the black asterisk
 282 marks the mean spectral reflectance for all features with $D > 20$ m.

283 3.3 Sub-feature variability

284 From these spectra, we observe that the spatially-averaged relationships tend to hold at individual
 285 scales: for features of a particular size, snowy features will be more reflective than bare features,
 286 with bare features especially lower in reflectance at the red/near-infrared wavelengths. However,
 287 we also find that the reflectance of snowy ice features tends to vary evenly with size across the
 288 visible and near-infrared wavelength range up to $D \approx 14$ m, at which point the spectral reflectance
 289 loses sensitivity to feature size and the spectra for $D \gtrsim 14$ m in Figure 13b overlap. Bare ice
 290 features behave quite differently (Figure 13a). All reflectance spectra show substantial decline in
 291 the near-infrared range, as one might expect from the spatially-averaged spectra shown in Figure
 292 9b and by merit of our very definition of a ‘bare’ feature (near-infrared to blue spectral reflectance
 293 ratio). However, reflectance does not increase monotonically with bare ice feature size; rather,
 294 reflectance peaks for features with $D \approx 18$ m- and the spectral reflectance averaged over all features

295 with $D > 20$ m is substantially lower in the near-infrared than all other spectra, offering insight into
 296 the nature of bare ice radiative signature variation with feature scale.



297 Our 3-class classification scheme simplifies the complex reality of the sea ice surface. In truth, an
 298 individually-identified contiguous feature may vary a great deal in its radiative properties over
 299 space. In order to describe this variation while keeping the clarifying simplicity of our feature
 300 categorization, we computed the inter-percentile (interquartile and interdecile) sub-feature
 301 variation as a function of feature scale (Figure 14). We find that variability in spectrally-averaged
 302 reflectance is significantly smaller across all features with $D < 6$ m than it is across larger
 303 features. For larger features ($D \geq 6$ m), the variation of spectrally-averaged reflectance is much
 304 greater for bare ice than for snowy ice.

305 4 Discussion

306 The satellite imagery in Figure 1 shows that the transition of the ice surface from predominantly
 307 snow-covered (white) to predominantly bare or ponded (grey or blue-green), a remarkable degree
 308 of melt and surface degradation occurred between 5/6/2019 and 5/9/2019, meaning that our aerial
 309 observations were made over ice that was in an advanced state of degradation. The relatively warm,
 310 moist air mass that arrived in the hours before 5/8/2019 may have been the principal culprit for
 311 this change. (Skylingstad & Polashenski, 2018) found that synoptic weather events transporting
 312 warm, moist air over sea ice (and driving sensible/latent heat flux) are the key trigger of incipient
 313 surface melt, after which changes to surface albedo result in solar radiation being the principal
 314 driver of heat uptake by the sea ice surface. Light transmittance and subsurface light absorption is
 315 markedly higher for first-year ice than for multi-year ice (Nicolaus et al., 2013). Furthermore, the
 316 sea ice in Kotzebue sound was qualitatively determined to be rich in sediment from the Kobuk and
 317 Noatak Rivers. The presence of sediment is understood to greatly enhance the absorption of solar

318 radiation across the visible and near-infrared wavelengths (Perovich, 2017). The absence of multi-
 319 year ice, abundance of sediment, and potentially widespread snow ice formations (Mahoney et al,
 320 2021) may all help to explain how the landfast ice progressed from snowy and white to rotten and
 321 broken in one week's time.

322 The radiometric observations performed as part of the present study were parsed along three
 323 principal axes: feature type (i.e., ponded ice, snowy ice, and bare ice), feature geometry (i.e., area,
 324 perimeter, or some derivative thereof), and wavelength (i.e., in a spectral sense). The simplest form
 325 of the results from this work is shown in Figure 9, where the variation of surface reflectance
 326 (wavelength-averaged and wavelength-dependent) is displayed as a function of net solar
 327 irradiance. The results of Figure 9a are intuitive, and in agreement with the findings of (Yackel et
 328 al., 2000): regions with a higher fraction of white/snowy ice have higher total surface reflectance
 329 and are associated with lower absorption of solar radiation. The surface reflectance spectra shown
 330 in Figure 9b offer a view of sea ice that is analogous to the one presented by (Grenfell & Perovich,
 331 1984), in which measurements of spectral albedo were performed over sea ice with a variety of
 332 surface types. For the bare ice and melt pond conditions similar to those observed during our field
 333 campaign, there was found to be a steep decline with wavelength for wavelengths between 600-
 334 800 nm, with white ice showing a far more gradual decline with wavelength.

335 Melt ponds draw a great amount of attention in the literature related to sea ice radiative properties-
 336 and for good reason. On thick, multi-year ice with persistent snow cover (and therefore generally
 337 high albedo across the visible spectrum), melt ponds represent islands of exceptional radiative
 338 penetration and under-ice heat absorption. The thin and degraded first-year ice of Kotzebue Sound
 339 that served as the subject of our observations in May 2019 held a vanishingly small number of
 340 melt ponds: less than 0.5% of the imaged surface area. Although the classification algorithm has
 341 been validated via in situ observations by other researchers (König & Oppelt, 2020), we did not
 342 perform any ground-truth measurements during our field observational period. It is therefore
 343 possible that our approach under-counted melt ponds. This may have impacted our ability to fully
 344 characterize melt pond fractal dimension: we did not observe a transition in melt pond fractal
 345 dimension from 1 to 2. This transition corresponds to ponds of increasingly serpentine, complex
 346 arrangement, and is often observed (Hohenegger et al., 2012) and reproduced via physical
 347 modeling (Bowen et al., 2018). Nevertheless, as shown in Figure 10, our observations of the melt
 348 pond spatial distribution showed good agreement with previous observations (Huang et al., 2016;
 349 Perovich, Tucker, et al., 2002) and the geometric model of (Popović et al., 2018).

350 The geometric analysis frameworks often applied to melt ponds is in fact well-suited towards the
 351 other surface types classified here: snowy & bare ice (Figure 11). For those surface types, we found
 352 that small, relatively dark features were most plentiful, with larger and more reflective features
 353 somewhat scarce. The behavior in these two feature size clusters appeared to follow two distinct
 354 power laws. For snowy features, these are $P(D) \propto D^{-1.3}$ for $2 \text{ m} < D < 5 \text{ m}$ and $P(D) \propto D^{-3.5}$
 355 for $10 \text{ m} < D < 20 \text{ m}$. The intermediate domain of $5 \text{ m} < D < 10 \text{ m}$ corresponds to a range in
 356 perimeter of 40 m – 80 m for a feature with area 100 m²; it is over this span of values that we also
 357 observe the transition of fractal dimension from approximately 1.25 to 1.37. This shift indicates
 358 that larger, more reflective snowy and bare ice surface features are more complex in shape than
 359 smaller, darker features- but only a bit more so. The analogous transition for melt ponds (Bowen
 360 et al., 2018; Hohenegger et al., 2012) is quite stark: from fractal dimension just above 1 (very
 361 nearly circular ponds) to fractal dimension approaching 2 (very nearly a space-filling curve). This

362 comparison indicates that, while feature complexity of bare and snowy ice surfaces increases with
363 size, it does so only up to a moderate level. This indicates that large features tend to be bulky, with
364 well-defined interior and exterior regions.

365 The reflectance spectra depicted in Figure 13 offer a more detailed view of these surface feature
366 characteristics. The spectra show an increase in snowy ice reflectance with feature sizes up to $D \approx$
367 14 m, with larger patches no longer varying with size in spectral reflectance. This is compatible
368 with our previous description of surface features as fairly simple in shape with well-defined
369 interior regions. The observed behavior for bare ice surfaces is quite different, varying non-
370 monotonically with feature size. For bare ice regions, reflectance increases with feature size up to
371 $D \approx 18$ m, only to *decrease* with size (especially in the near-infrared range). This reduction appears
372 to become substantial for the features with $D > 20$ m, patches which constitute over 55% of the
373 total observed bare ice by area. As discussed earlier in this section, it may be the case that our
374 classification scheme is under-detecting ponded sea ice. However, the stark difference between
375 snowy and bare reflectance spectra indicate that we are identifying meaningfully different surface
376 types, even if there is some uncertainty regarding the identification of melt ponds.

377 The sub-region variability in reflectance (Figure 14) provides a complementary description of this
378 distinction. For both bare and snowy surfaces, variability in reflectance increases with scale as
379 features begin to develop fringes, tapering off as darker fringes become a smaller portion of the
380 overall feature area. The scale dependence of this effect appears coincident with the power law
381 and fractal dimension transition scales, shoring up the interpretation that small, loosely-connected
382 regions of uniformly-low reflectance are plentiful. However, these small features still represent a
383 small fraction of the overall sea ice surface area. In order to provide a broader view of the observed
384 sea ice radiative characteristics, it is important to also consider large patches which are few in
385 number but great in total surface area. Snowy ice features increase in mean reflectance (and relative
386 variability) with up to some critical scale at which the patch interior is sufficiently protected from
387 the darker, more absorptive patch fringes. For bare ice features, however, the largest regions which
388 occupy the bulk of the bare ice surface area are darker, of higher variability, and of particularly
389 low reflectivity in the near-infrared. Based on the highly variable reflectance observed for the
390 largest patches, it may be that these regions include cracks, melt water, suspended sediment, and
391 other characteristics which render them vulnerable to increasing absorption of solar radiation.

392 These findings suggest that surface feature geometry has a meaningful impact on the degree to
393 which sea ice reflects incoming solar radiation. We expect that efforts which seek to model changes
394 to Earth's climate will be advanced by incorporation of these effects, and we eagerly anticipate
395 future studies which investigate the scale-dependence of ice-albedo feedback mechanisms.
396 Indigenous communities who rely on the sea ice as part of their way of life may benefit from such
397 improvements to climate forecasting capabilities. Furthermore, quantification of solar radiation
398 uptake that is dependent upon sea ice color and feature size may assist in the determination of
399 structural safety for use in travel and hunting activities.

400 **5 Conclusions**

401 We performed a series of aerial observations of sea ice radiative properties at an advanced stage
402 of melt and breakup. These observations were performed in Kotzebue Sound, Alaska, and occurred
403 in the context of knowledge co-production with with Elders from Kotzebue (study co-authors J.G.,

404 C.H., R.J.S., and R.S., Sr.). This collaboration began with the initial project conception, continuing
405 through execution of observations, and extending into analysis. Our observations allowed us to
406 quantify the mean solar radiative flux into the sea ice as a function of both ice color and spectral
407 surface reflectance. Using high-resolution hyperspectral radiometric imaging, we were able to
408 reconstruct maps of spectral reflectance over the visible to near-infrared range at spatial scales
409 down to 50 cm. This dataset was used to classify the surface into regions of melt ponds, bare ice,
410 and snowy ice and to perform geometric analyses on those regions across the resolved spectrum.
411 Melt ponds were scarce during our operating period, though the ponds we did observe presented
412 with a scale distribution that agreed with that of previous observations and modeling. The spectral
413 reflectance of snowy ice was found to vary with feature size, increasing until moderate scale and
414 then ceasing to vary at all.

415 These observations of surface reflectance variation offer insight into the role that feature size
416 distribution and geometry play in the overall radiative balance of sea ice. Diminished surface
417 reflectance leads to enhanced uptake of solar radiation, which in turn hastens the degradation (and
418 ultimately, breakup) of the sea ice. We expect that the size and geometry dependence of surface
419 reflectance works to strengthen positive feedbacks associated with radiation uptake. In short: the
420 tendency of large blue-green features to absorb radiation increases with their size, while large
421 snowy features absorb more solar radiation as they are subdivided and split by melt and
422 degradation. We recognize that climate models cannot afford to directly resolve individual features
423 on the sea ice. However, we hope that the effects described in this paper can be parameterized
424 statistically, incorporating scale-aware feedbacks into models without the need for directly
425 resolving individual features.

426 In closing, these observations provide a quantitative description of the radiative and geometric
427 properties of features on the surface of first-year sea ice undergoing the late stages of melt and
428 breakup. Although the observational period was short, the high spatial and spectral resolutions of
429 the sensing approach deployed here have yielded a rich characterization of the sea ice surface. We
430 anticipate that the results of this work will be used to inform future, larger-scale field observational
431 and modeling efforts aimed at providing a comprehensive description of the sea ice surface
432 properties.

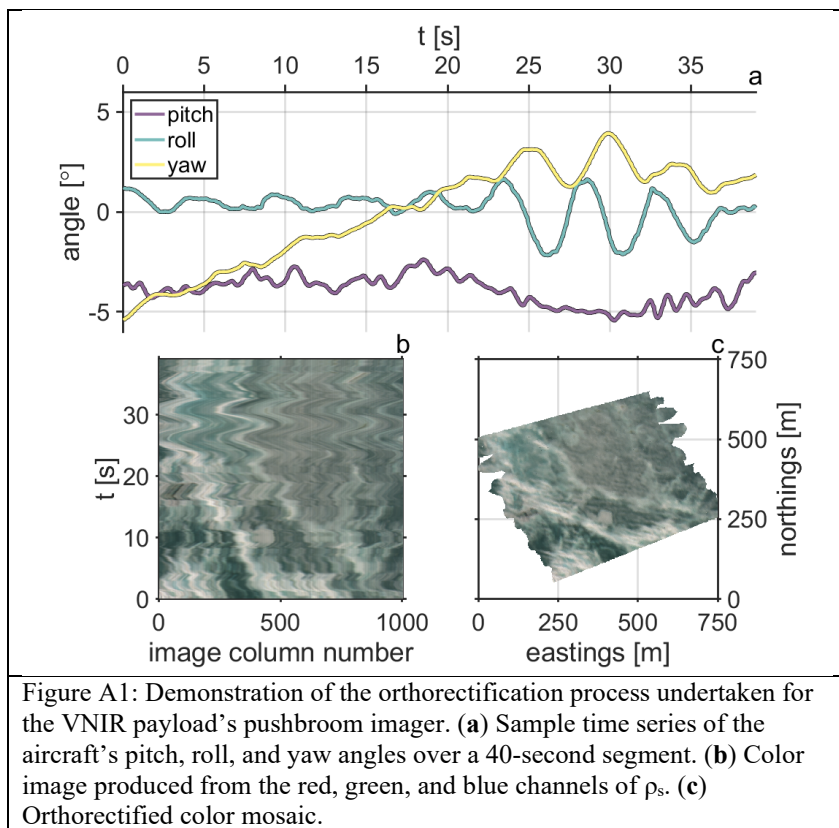
433 **Acknowledgments**

434 This work was supported by a grant from the Gordon and Betty Moore Foundation. We are grateful
435 to the Qikiqtaġruṅmiut people and community of Kotzebue, Alaska. The sharing of their
436 Indigenous Knowledge was an integral part of the design and execution of this work. We thank
437 the Native Village of Kotzebue and the University of Alaska Fairbanks (Chukchi campus) who
438 provided meeting facilities and the US Fish and Wildlife Selawik Refuge, who provided crucial
439 logistical support. We thank Scott Brown, Tej Dhakal, and Ryan Harris for their engineering
440 expertise in the development and field operation of the scientific payloads. We thank Cory Rosene,
441 Scott Bowers, and Sean Culbertson for their work in piloting and maintaining the aircraft.
442 Historical meteorological data from the Kotzebue airport were obtained from the National Centers
443 for Environmental Information at [https://www.ncdc.noaa.gov/cdo-
444 web/datasets/LCD/stations/WBAN:26616/detail](https://www.ncdc.noaa.gov/cdo-web/datasets/LCD/stations/WBAN:26616/detail). The terrestrial and UAV-obtained datasets (as
445 well as all computer codes used to process them to produce the figures shown in this document)

446 are available through the Columbia Academic Commons (DOI: 10.7916/rrbv-k026). The authors
447 declare that they have no competing financial interests.
448

449 **Appendix**

450 The TSPI solution produced through post-processing of data obtained from the Base payload's
 451 INU provided the aircraft position and attitude at 50 Hz. This was interpolated onto the time vector
 452 of the radiometric instrumentation of the VNIR payload. Three attitude angles- pitch, roll, and
 453 yaw- are shown in Figure A1a; note that the yaw angle represents variation about the mean
 454 heading. An RGB representation of 60 seconds' worth of calibrated (but not georectified) surface
 455 reflectance data is shown in Figure A1b. Vectors originating from the camera focal point and
 456 terminating at each point in this array were initialized; the position corresponding to each spatial
 457 measurement of surface reflectance was determined by rotating each vector by the instantaneous
 458 UAV attitude in three dimensions and finding its intersection with the ellipsoid defining the mean
 459 ocean surface. The output of this process is shown in Figure A1c. Another illustration of this VNIR
 460 pushbroom orthrectification is provided by (Zappa et al., 2020).



461

462

463

464 **References**

- 465 Barber, D. G., & Yackel, J. (2010). The physical, radiative and microwave scattering characteristics of melt ponds
466 on Arctic landfast sea ice. *International Journal of Remote Sensing*, 20(10), 2069–2090.
467 <https://doi.org/10.1080/014311699212353>
- 468 Bourassa, M. A., Gille, S. T., Bitz, C., Carlson, D., Cerovecki, I., Clayson, C. A., et al. (2013). High-Latitude Ocean
469 and Sea Ice Surface Fluxes: Challenges for Climate Research. *Bulletin of the American Meteorological*
470 *Society*, 94(3), 403–423. <https://doi.org/10.1175/BAMS-D-11-00244.1>
- 471 Bowen, B., Strong, C., & Golden, K. M. (2018). Modeling the fractal geometry of Arctic melt ponds using the level
472 sets of random surfaces. *Journal of Fractal Geometry*, 5(2), 121–142. <https://doi.org/10.4171/JFG/58>
- 473 Bremer, S., Wardekker, A., Dessai, S., Sobolowski, S., Slaattelid, R., & van der Sluijs, J. (2019). Toward a multi-
474 faceted conception of co-production of climate services. *Climate Services*, 13, 42–50.
475 <https://doi.org/10.1016/J.CLISER.2019.01.003>
- 476 Brennan, M. K., Hakim, G. J., & Blanchard-Wrigglesworth, E. (2020). Arctic Sea-Ice Variability During the
477 Instrumental Era. *Geophysical Research Letters*, 47(7), e2019GL086843.
478 <https://doi.org/10.1029/2019GL086843>
- 479 Budyko, M. I. (1969). The effect of solar radiation variations on the climate of the Earth. *Tellus*, 21(5).
- 480 Carmack, E., Polyakov, I., Padman, L., Fer, I., Hunke, E., Hutchings, J., et al. (2015). Toward Quantifying the
481 Increasing Role of Oceanic Heat in Sea Ice Loss in the New Arctic. *Bulletin of the American*
482 *Meteorological Society*, 96(12), 2079–2105. <https://doi.org/10.1175/BAMS-D-13-00177.1>
- 483 Dai, A., Luo, D., Song, M., & Liu, J. (2019). Arctic amplification is caused by sea-ice loss under increasing CO 2.
484 *Nature Communications 2019 10:1*, 10(1), 1–13. <https://doi.org/10.1038/s41467-018-07954-9>
- 485 David-Chavez, D. M., & Gavin, M. C. (2018). A global assessment of Indigenous community engagement in
486 climate research. *Environmental Research Letters*, 13(12), 123005. [https://doi.org/10.1088/1748-](https://doi.org/10.1088/1748-9326/AAF300)
487 [9326/AAF300](https://doi.org/10.1088/1748-9326/AAF300)
- 488 Ehn, J. K., Mundy, C. J., Barber, D. G., Hop, H., Rossnagel, A., & Stewart, J. (2011). Impact of horizontal spreading
489 on light propagation in melt pond covered seasonal sea ice in the Canadian Arctic. *Journal of Geophysical*
490 *Research: Oceans*, 116(C9), 0–02. <https://doi.org/10.1029/2010JC006908>

- 491 Eicken, H. (2010). Indigenous Knowledge and Sea Ice Science: What Can We Learn from Indigenous Ice Users?
492 *SIKU: Knowing Our Ice: Documenting Inuit Sea Ice Knowledge and Use*, 357–376.
493 https://doi.org/10.1007/978-90-481-8587-0_15
- 494 Eicken, H., Danielsen, F., Sam, J.-M., Fidel, M., Johnson, N., Poulsen, M. K., et al. (2021). Connecting Top-Down
495 and Bottom-Up Approaches in Environmental Observing. *BioScience*, 71(5), 467–483.
496 <https://doi.org/10.1093/BIOSCI/BIAB018>
- 497 Frey, K. E., Perovich, D. K., & Light, B. (2011). The spatial distribution of solar radiation under a melting Arctic
498 sea ice cover. *Geophysical Research Letters*, 38(22). <https://doi.org/10.1029/2011GL049421>
- 499 Gearheard, S. F., Leavitt, J. M., Mahoney, A. R., Opie, M., Oshima, T., & Sanguya, J. (Eds.). (2013). *The Meaning*
500 *of Ice: People and Sea Ice in Three Arctic Communities*. International Polar Institute Press.
- 501 Grenfell, T. C., & Perovich, D. K. (1984). Spectral albedos of sea ice and incident solar irradiance in the southern
502 Beaufort Sea. *Journal of Geophysical Research: Oceans*, 89(C3), 3573–3580.
503 <https://doi.org/10.1029/JC089IC03P03573>
- 504 Grenfell, T. C., & Perovich, D. K. (2004). Seasonal and spatial evolution of albedo in a snow-ice-land-ocean
505 environment. *Journal of Geophysical Research: Oceans*, 109(C1), 1001.
506 <https://doi.org/10.1029/2003JC001866>
- 507 Hauser, D. D. W., Whiting, A. V., Mahoney, A. R., Goodwin, J., Harris, C., Schaeffer, R. J., et al. (2021). Co-
508 production of knowledge reveals loss of Indigenous hunting opportunities in the face of accelerating Arctic
509 climate change. *Environmental Research Letters*, 16(9), 095003. [https://doi.org/10.1088/1748-](https://doi.org/10.1088/1748-9326/AC1A36)
510 [9326/AC1A36](https://doi.org/10.1088/1748-9326/AC1A36)
- 511 Hohenegger, C., Alali, B., Steffen, K. R., Perovich, D. K., & Golden, K. M. (2012). Transition in the fractal
512 geometry of Arctic melt ponds. *The Cryosphere*, 6(5), 1157–1162. <https://doi.org/10.5194/tc-6-1157-2012>
- 513 Horvat, C., Flocco, D., Rees Jones, D. W., Roach, L., & Golden, K. M. (2020). The Effect of Melt Pond Geometry
514 on the Distribution of Solar Energy Under First-Year Sea Ice. *Geophysical Research Letters*, 47(4),
515 e2019GL085956. <https://doi.org/10.1029/2019GL085956>
- 516 Huang, W., Lu, P., Lei, R., Xie, H., & Li, Z. (2016). Melt pond distribution and geometry in high Arctic sea ice
517 derived from aerial investigations. *Annals of Glaciology*, 57(73), 105–118.
518 <https://doi.org/10.1017/AOG.2016.30>

- 519 Klenk, N., Fiume, A., Meehan, K., & Gibbes, C. (2017). Local knowledge in climate adaptation research: moving
520 knowledge frameworks from extraction to co-production. *Wiley Interdisciplinary Reviews: Climate*
521 *Change*, 8(5), e475. <https://doi.org/10.1002/WCC.475>
- 522 Klinkenberg, B. (1994). A review of methods used to determine the fractal dimension of linear features.
523 *Mathematical Geology*, 26(1), 23–46. <https://doi.org/10.1007/BF02065874>
- 524 König, M., & Oppelt, N. (2020). A linear model to derive melt pond depth on Arctic sea ice from hyperspectral data.
525 *Cryosphere*, 14(8), 2567–2579. <https://doi.org/10.5194/TC-14-2567-2020>
- 526 Kwok, R., & Rothrock, D. A. (2009). Decline in Arctic sea ice thickness from submarine and ICESat records: 1958–
527 2008. *Geophysical Research Letters*, 36(15). <https://doi.org/10.1029/2009GL039035>
- 528 Light, B., Grenfell, T. C., & Perovich, D. K. (2008). Transmission and absorption of solar radiation by Arctic sea ice
529 during the melt season. *Journal of Geophysical Research: Oceans*, 113(C3), 3023.
530 <https://doi.org/10.1029/2006JC003977>
- 531 Light, B., Perovich, D. K., Webster, M. A., Polashenski, C., & Dacic, R. (2015). Optical properties of melting first-
532 year Arctic sea ice. *Journal of Geophysical Research: Oceans*, 120(11), 7657–7675.
533 <https://doi.org/10.1002/2015JC011163>
- 534 Lindsay, J. M., Hauser, D. D. W., Mahoney, A. R., Laidre, K. L., Goodwin, J., Harris, C., et al. (2023).
535 Characteristics of ringed seal *Pusa hispida* ('natchiq') denning habitat in Kotzebue Sound, Alaska, during a
536 year of limited sea ice and snow. *Marine Ecology Progress Series*, 705, 1–20.
537 <https://doi.org/10.3354/meps14252>
- 538 Lu, P., Leppäranta, M., Cheng, B., & Li, Z. (2016). Influence of melt-pond depth and ice thickness on Arctic sea-ice
539 albedo and light transmittance. *Cold Regions Science and Technology*, 124, 1–10.
540 <https://doi.org/10.1016/J.COLDREGIONS.2015.12.010>
- 541 Mahoney, A. R., Turner, K. E., Hauser, D. D. W., Laxague, N. J. M., Lindsay, J. M., Whiting, A. V., et al. (2021).
542 Thin ice, deep snow and surface flooding in Kotzebue Sound: landfast ice mass balance during two
543 anomalously warm winters and implications for marine mammals and subsistence hunting. *Journal of*
544 *Glaciology*, 67(266), 1013–1027. <https://doi.org/10.1017/JOG.2021.49>

- 545 Markus, T., Stroeve, J. C., & Miller, J. (2009). Recent changes in Arctic sea ice melt onset, freezeup, and melt
546 season length. *Journal of Geophysical Research: Oceans*, *114*(C12), 12024.
547 <https://doi.org/10.1029/2009JC005436>
- 548 Nicolaus, M., Arndt, S., Katlein, C., Maslanik, J., & Hendricks, S. (2013). Changes in Arctic sea ice result in
549 increasing light transmittance and absorption. *Geophysical Research Letters*, *40*(11), 2699–2700.
550 <https://doi.org/10.1002/GRL.50523>
- 551 Overland, J. E. (2020). Less climatic resilience in the Arctic. *Weather and Climate Extremes*, *30*, 100275.
552 <https://doi.org/10.1016/J.WACE.2020.100275>
- 553 Perovich, D. K. (2017). Sea ice and sunlight. *Sea Ice: Third Edition*, 110–137.
554 <https://doi.org/10.1002/9781118778371.CH4>
- 555 Perovich, D. K., & Polashenski, C. (2012). Albedo evolution of seasonal Arctic sea ice. *Geophysical Research
556 Letters*, *39*(8), 8501. <https://doi.org/10.1029/2012GL051432>
- 557 Perovich, D. K., Roesler, C. S., & Pegau, W. S. (1998). Variability in Arctic sea ice optical properties. *Journal of
558 Geophysical Research: Oceans*, *103*(C1), 1193–1208. <https://doi.org/10.1029/97JC01614>
- 559 Perovich, D. K., Tucker, W. B., & Ligett, K. A. (2002). Aerial observations of the evolution of ice surface
560 conditions during summer. *Journal of Geophysical Research: Oceans*, *107*(C10), SHE 24-1.
561 <https://doi.org/10.1029/2000JC000449>
- 562 Perovich, D. K., Grenfell, T. C., Light, B., & Hobbs, P. V. (2002). Seasonal evolution of the albedo of multiyear
563 Arctic sea ice. *Journal of Geophysical Research: Oceans*, *107*(C10), SHE 20-1.
564 <https://doi.org/10.1029/2000JC000438>
- 565 Perovich, D. K., Light, B., & Dickinson, S. (2020). Changing ice and changing light: trends in solar heat input to the
566 upper Arctic ocean from 1988 to 2014. *Annals of Glaciology*, *61*(83), 401–407.
567 <https://doi.org/10.1017/AOG.2020.62>
- 568 Planck, C. J., Perovich, D. K., & Light, B. (2020). A Synthesis of Observations and Models to Assess the Time
569 Series of Sea Ice Mass Balance in the Beaufort Sea. *Journal of Geophysical Research: Oceans*, *125*(11),
570 e2019JC015833. <https://doi.org/10.1029/2019JC015833>
- 571 Popović, P., Cael, B. B., Silber, M., & Abbot, D. S. (2018). Simple Rules Govern the Patterns of Arctic Sea Ice Melt
572 Ponds. *Physical Review Letters*, *120*(14), 148701. <https://doi.org/10.1103/PhysRevLett.120.148701>

- 573 Rantanen, M., Karpechko, A. Y., Lipponen, A., Nordling, K., Hyvärinen, O., Ruosteenoja, K., et al. (2022). The
574 Arctic has warmed nearly four times faster than the globe since 1979. *Communications Earth &*
575 *Environment*, 3(1), 1–10. <https://doi.org/10.1038/s43247-022-00498-3>
- 576 Screen, J. A., & Simmonds, I. (2010). The central role of diminishing sea ice in recent Arctic temperature
577 amplification. *Nature*, 464(7293), 1334–1337. <https://doi.org/10.1038/nature09051>
- 578 Skyllingstad, E. D., & Polashenski, C. (2018). Estimated Heat Budget During Summer Melt of Arctic First-Year Sea
579 Ice. *Geophysical Research Letters*, 45(21), 11,789–11,797. <https://doi.org/10.1029/2018GL080349>
- 580 Stroeve, J. C., Markus, T., Boisvert, L., Miller, J., & Barrett, A. (2014). Changes in Arctic melt season and
581 implications for sea ice loss. *Geophysical Research Letters*, 41(4), 1216–1225.
582 <https://doi.org/10.1002/2013GL058951>
- 583 Witte, C. R., Zappa, C. J., Mahoney, A. R., Goodwin, J., Harris, C., Schaeffer, R. J., et al. (2021). The Winter Heat
584 Budget of Sea Ice in Kotzebue Sound: Residual Ocean Heat and the Seasonal Roles of River Outflow.
585 *Journal of Geophysical Research: Oceans*, 126(9), e2020JC016784. <https://doi.org/10.1029/2020JC016784>
- 586 Wright, N. C., & Polashenski, C. M. (2018). Open-source algorithm for detecting sea ice surface features in high-
587 resolution optical imagery. *The Cryosphere*, 12(4), 1307–1329. <https://doi.org/10.5194/tc-12-1307-2018>
- 588 Yackel, J. J., Barber, D. G., & Hanesiak, J. M. (2000). Melt ponds on sea ice in the Canadian Archipelago: 1.
589 Variability in morphological and radiative properties. *Journal of Geophysical Research: Oceans*, 105(C9),
590 22049–22060. <https://doi.org/10.1029/2000JC900075>
- 591 Yua, E., Raymond-Yakoubian, J., Daniel, R., & Behe, C. (2022). A framework for co-production of knowledge in
592 the context of Arctic research. *Ecology and Society*, 27(1). <https://doi.org/10.5751/ES-12960-270134>
- 593 Zappa, C. J., Brown, S. M., Laxague, N. J. M., Dhakal, T., Harris, R. A., Farber, A. M., & Subramaniam, A. (2020).
594 Using Ship-Deployed High-Endurance Unmanned Aerial Vehicles for the Study of Ocean Surface and
595 Atmospheric Boundary Layer Processes. *Frontiers in Marine Science*, 6, 777.
596 <https://doi.org/10.3389/fmars.2019.00777>

597